Materials & Design 221 (2022) 110949

Contents lists available at ScienceDirect

Materials & Design

journal homepage: www.elsevier.com/locate/matdes

Friction stir welding of SS 316 LN and Nitronic 50 jacket sections for application in superconducting fusion magnet systems

Supreeth Gaddam [a,b], Ravi Sankar Haridas [a,b], Charlie Sanabria [c], Deepthi Tammana [c], Diana Berman [b], Rajiv S. Mishra [a,b,*]

[a] Center for Friction Stir Processing, Department of Materials Science and Engineering, University of North Texas, Denton, TX 76207, USA
[b] Advanced Materials and Manufacturing Processes Institute, University of North Texas, Denton, TX 76207, USA
[c] Commonwealth Fusion Systems, Cambridge, MA, USA

HIGHLIGHTS

- Jackets for superconducting cables successfully fabricated with friction stir welding.
- The welded SS 316 LN has high strength and conducive magnetic properties.
- Relevant for jackets of cable-in-conduit conductors (CICCs) in tokamak type reactors.

GRAPHICAL ABSTRACT

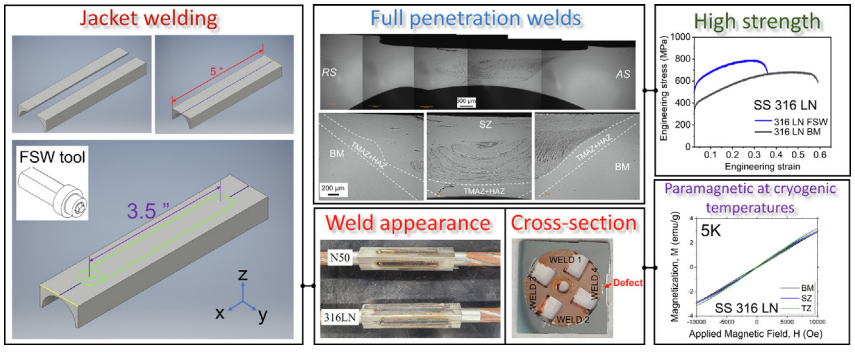

ARTICLE INFO

Article history:
Received 27 May 2022
Revised 10 July 2022
Accepted 11 July 2022
Available online 14 July 2022

Keywords:
Friction stir welding (FSW)
SS 316 LN
Nitronic 50
Nuclear fusion
Cable-in-conduit conductor jacket

ABSTRACT

This study explored the possibility of using friction stir welding (FSW) to join jacket web sections of two nitrogen-containing stainless steels for housing internally cooled superconducting cables which are utilized to generate magnetic fields in tokamak type fusion reactor systems. The two candidate materials chosen for the jacket are SS 316 LN and Nitronic – 50 owing to their desirable mechanical and physical properties at cryogenic service temperature. The current manufacturing techniques to fabricate the jackets or conduits include fusion butt welding. There are some inherent disadvantages of utilizing the fusion joining process such as the possibility of sensitization and the evolution of undesirable phases detrimental to the application. An attempt has been made to fabricate the jackets with FSW to evaluate its feasibility to obtain the desired mechanical and physical properties critical to the application. The welding parameters optimization, workpiece clamping approach, microstructure evolution, hardness line profiles, tensile properties, and magnetic properties of the jacket welds corresponding to both the materials have been discussed in the paper. It has been shown that the FSW fabricated SS 316 LN jackets possessed the required strength and magnetic properties critical to this application.

1. Introduction

Tokamak type nuclear fusion reactors work on the principle of containing a donut-shaped plasma within a toroidal-shaped magnetic field [1]. Several experimental tokamaks are being developed

* Corresponding author at: Center for Friction Stir Processing, Department of Materials Science and Engineering, University of North Texas, Denton, TX 76207, USA.
E-mail address: rajiv.mishra@unt.edu (R.S. Mishra).

https://doi.org/10.1016/j.matdes.2022.110949
0264-1275/

around the world to better understand the science behind nuclear fusion-based energy generation. The International Thermonuclear Experimental Reactor (ITER) in France [2] and the SPARC reactor in the US [3] are two of the notable programs around the world that are in pursuit of reaching a break-even condition with their experiments. The nuclear fusion-based energy generation technology would be crucial to the entire world to meet the long-term planetary goals of various climate change accords such as the 2016 Paris Climate Agreement and the United Nations Climate Change Conference (COP) goals [4,5].

One of the crucial technologies that will enable the success of nuclear fusion-based energy generation is the superconducting magnet systems used to contain and control the super-hot plasma. Internally cooled cable-in-conduit conductors (CICC), which comprise of wound coils of superconducting material on a copper cable, are utilized to produce the magnetic fields in a tokamak [3,6]. These CICCs are comprised of electrical elements (superconductors and copper), cooling elements (often in the form of a central cooling channel) and structural elements which are in most cases made of stainless steel. A cryogenic fluid is passed through the cable during operation to maintain superconductivity as a high current density is passed through to generate a very strong magnetic field around it [6]. Whenever radial plates are not used, the outer part of the cable, often referred to as the 'jacket', is the main component providing structural rigidity to the magnets [7–9]. In the case of the SPARC Central Solenoid (or CS, one of the magnet systems of a tokamak), the conductor of choice is a recently developed CICC called VIPER, which has been jointly developed by the MIT Plasma Science and Fusion Center and Commonwealth Fusion Systems (CFS) in Cambridge, MA. The details of the configuration, construction, and performance of the cable are presented by Hartwig et al. [10].

The jacket material must withstand the high stresses exerted by the Lorentz force produced during operation and be least detrimental to the induced magnetic field [11,12]. This can be achieved only when the material is strong enough and all the phases in the material are paramagnetic in nature, where the induced dipoles reorient randomly after the external magnetic field has been removed [13]. Considering these structural and functional requirements, SS 316 LN and Nitronic-50 (N50) are two candidate materials suitable for the jacket application as they possess the strength and magnetic properties required at cryogenic (4 K – 77 K) service temperature [14,15]. The key characteristic of these materials is the ability to retain the austenitic γ-phase which is paramagnetic even at cryogenic temperatures. The high percentage of nitrogen promotes the stability of the γ-phase at cryogenic temperatures [16,17]. The current technique to produce the jackets involves compaction rolling and fusion butt welding of jacket sections [18]. Fusion welding of the materials under investigation has been shown to induce certain undesirable properties into the materials, such as sensitization in the heat-affected zone (HAZ) and the evolution of δ-ferrite in the weld nugget [19–24]. δ-ferrite is a ferromagnetic phase which would lead to a higher degree of magnetization of the jacket material. This magnetization will interfere with the induced magnetic fields of the internal coils and lead to issues with the containment of the plasma within the tokamak [25].

To address the shortcomings of the fusion welding process, there have been alternative approaches adopted to join the sections of a jacket together. One such attempt was made by Decool et al. [12] where they utilized explosive bonding technique to manufacture twin-boxes that housed the cables. This technique would not be suitable for a single CICC assembly and therefore has its own set of limitations. In the current study, friction stir welding (FSW) approach was adopted to join the jacket sections together to form the conduit to house the internal cable.

To evaluate the feasibility of FSW to join the two candidate materials – SS 316 LN and N50 – a series of experiments and characterization tasks were carried out. The first step involved the design of a suitable FSW tool which was made using a W-Re alloy. The next step involved the optimization of welding parameters to obtain a full penetration weld without defects. The subsequent steps involved the welding of the jacket sections and evaluation of the welds by microstructural analysis. Finally, the tensile behavior, hardness line profiles, and magnetic properties of different regions of the welded materials were also evaluated.

There have been several reports establishing the feasibility and advantages of FSW to join ferrous alloys with similar compositions utilized in this work [26–28]. This study is application specific to evaluate the suitability of the FSW approach to fabricate SS 316 LN and N50 jackets for CICC application. However, the results presented here will help extend the understanding in literature by evaluating magnetic properties of the FSW weldments which is critical to the intended application in nuclear fusion systems. Since SS 316 LN and Nitronic series alloys are used extensively in nuclear fusion systems for various structural applications [29,30], the data presented and discussed in this paper can potentially open new doors to adapt FSW to fabricate other critical components in nuclear fusion systems.

2. Materials and methods

The materials used in the present study were 1.5 mm thick sheets and jacket web sections of austenitic stainless steel SS 316 LN and Nitronic 50 (N50). The jacket web sections were fabricated at the Commonwealth Fusion Systems (CFS), Cambridge, MA. The dimensions of the jacket web sections are included in Fig. 1 (a). The nominal compositions of both the materials utilized in the study are presented in Table 1. The microstructure and EDS spectra corresponding to both the base materials are presented in Fig. 2. The tool utilized in the present study was made from W – 25 wt % Re with a tool geometry depicted in Fig. 1 (b) and was manufactured at Joining Innovations, LLC, Wichita, KS. Argon shielding gas was utilized to prevent oxidation of the weld surface and the tool. Bead-on-plate runs were performed on the 1.5 mm thick sheets for process parameter optimization with an emphasis on the downward forge force and peak temperature below the sheets. The temperature measurements were taken using K-type thermocouples located at three locations beneath the processed regions underneath a 0.072 mm stainless steel shim as depicted in Fig. 1 (c). With the optimized parameters, which are listed in Table 2, FSW runs were carried out on the jacket sections using the clamping approach shown in Fig. 3 (b, c). Four different welding runs were performed to join all four jacket sections over the central solenoid cable.

Transverse cross sections were obtained from the jacket-on-cable assemblies using a precision abrasive saw, Buehler IsoMet (Buehler Company, Lake Bluff, IL), for macro and microstructural analysis. Specimens for metallographic examination were further prepared using SiC polishing papers ranging from coarse to fine grit sizes followed by cloth polishing with a 1 μm diamond suspension and then finally with a 0.05 μm colloidal silica suspension in a vibratory polisher, Buehler VibroMet (Buehler Company, Lake Bluff, IL). Electro-etching with 10% oxalic acid solution (5 V, 10–15 sec, room temp.) was used to etch the jacket section welds for macrostructural investigation. Specific regions of the welded samples were examined in detail in the as-polished condition with electron backscatter diffraction (EBSD) on an FEI Nova NanoSEM 230 (FEI Company, Hillsboro, OR) equipped with a field emission source operated at an accelerating voltage of 20 kV and a spot size

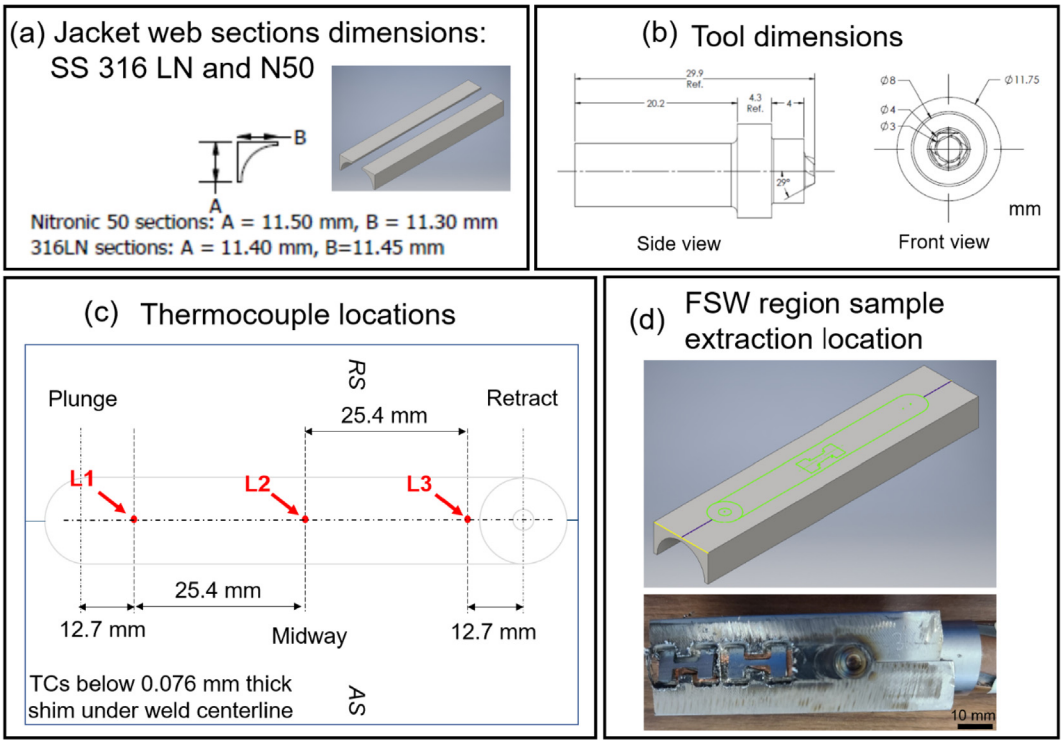

Fig. 1. (a) SS 316 LN and N50 jacket web dimensions, (b) dimensions of the tool used, (c) thermocouple locations for temperature measurements during the FSW run, and (d) schematic showing the region of mini-tensile sample extraction from the weld.

Table 1
Nominal compositions of the SS 316 LN and N50 base materials used in the study.

	C	Si	Mn	S	Cr	Ni	Mo	N	Co	P	Fe
SS 316 LN (wt. %)	<0.03	≤ 0.75	≤ 2.0	≤ 0.03	16.0–18.0	11.0–14.0	2.0–3.0	0.14–0.18	≤ 0.05	≤ 0.045	Bal.
N50 (wt. %)	≤ 0.06	≤ 1.0	4.0–6.0	≤ 0.03	20.5–23.5	11.5–13.5	1.5–3.0	0.20–0.40	–	–	Bal.

of 6. Scans were acquired at step sizes between 0.1 and 0.5 μm on a hexagonal grid.

Further, hardness line profiles were generated along the mid-sections of both the welded materials at a test load of 100 gf and a dwell time of 10 s with an indent spacing of 250 μm using a Buehler Wilson VH3300 auto hardness tester (Buehler Company, Lake Bluff, IL). Mini tensile specimens were milled out of the welded jacket sections (both from the base material region and the FSW region) using a Tormach PCNC 440 CNC mill (Tormach Company, Monona, WI). To characterize the tensile properties, mini-tensile samples based on the sub-sized ASTM E8 sample geometry were prepared and tested. Further details of the mini-tensile sample geometry can be found elsewhere [31]. The dimensions of the mini tensile specimen were 5 mm gauge length, ~1 mm width, and ~ 0.75 mm thickness. The tensile tests were carried out at an initial strain rate of 10^{-3} s^{-1}. The tensile data is presented only for the plastic region to account for machine rigidity issues in the elastic deformation regime. The samples corresponding to the FSW region were sectioned from the welded jackets as shown in Fig. 1 (d). Finally, magnetic properties – magnetization, M (emu/g) v/s temperature, T (from T = 5 K to 300 K, at 500 Oe applied magnetic field) and magnetization, M (emu/g) v/s applied magnetic field, H (Oe) (at T = 5 K, 77 K, and 300 K) - were computed for both the welded materials at different regions of each weld using the DynaCool Physical Property Measurement System (PPMS) (Quantum Design Inc, San Diego, CA) with a vibrating sample magnetometer (VSM) option. For this, the samples (~0.15 g in mass) were fixed to the quartz rod and tested.

3. Results and discussion

3.1. Process parameter optimization

To find suitable process parameters for FSW, bead-on-plate runs were made on the 1.5 mm thick sheets of SS 316 LN and N50 materials with spindle speeds 600, 800, and 1000 RPM at a constant traverse speed of 50.8 mm/minute, a plunge depth of 1.35 mm, a plunge velocity of 1 mm/min, and a spindle tilt of −1.5°. The goal was to obtain a full penetration weld without any defects while keeping the peak temperature as low as possible, and simultaneously keeping the forge force acting on the sheets low to avoid any sort of warping and deflection that are commonly observed during FSW of thin cross-section samples. It was experimentally observed that the 600 RPM, 50.8 mm/minute, −1.5° set of process parameters worked best for the SS 316 LN material and 800 RPM, 50.8 mm/minute, −1.5° set of process parameters worked best for the N50 material. The set of optimized parameters and process variable responses (forge force, spindle torque, and temperature) are presented in Table 2 and Fig. 4, respectively. It was observed that the peak temperature beneath the processed regions at three different locations reached 605°C ± 5°C for the SS 316 LN run and

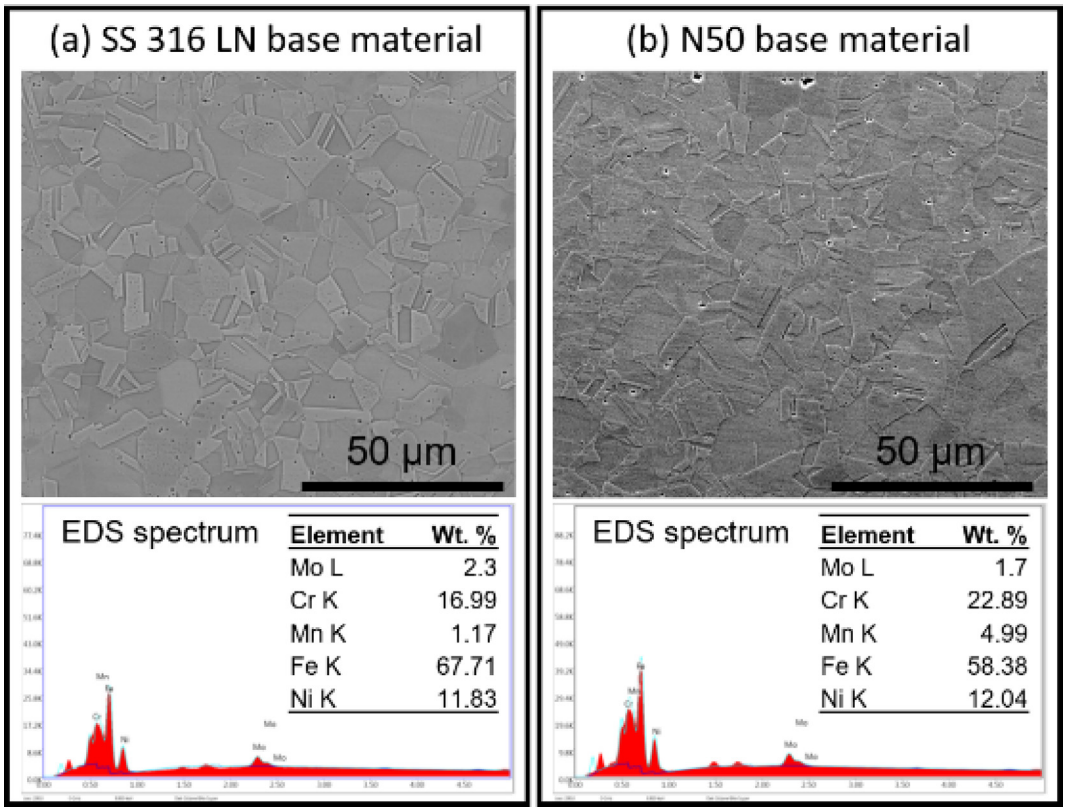

Fig. 2. SEM micrographs and EDS spectra of the (a) SS 316 LN and (b) N50 base materials.

Table 2
Optimized FSW process parameters for both steels.

Material	Rotational speed (RPM)	Plunge speed (mm/min)	Plunge depth (mm)	Traverse speed (mm/min)	Tile angle (degrees)
SS 316 LN	600	1	1.35	50.8	−1.5
Nitronic 50 (N50)	800	1	1.35	50.8	−1.5

635C ± 30C for the N50 run as seen in Fig. 4 (a1 and b1). The peak force recorded during the SS 316 LN run was 5168 N (Fig. 4 (a2)) and the peak force recorded during the N50 run was 4850 N (Fig. 4 (b2)). The peak forces are observed when the tool shoulder makes first contact with the workpiece material. The average traverse forces were much lower at 3237 N for the SS 316 LN run (Fig. 4 (a2)) and 3259 N for the N50 run (Fig. 4 (b2)). The lower spindle torque values observed in the N50 weld also indicate that the temperatures within the material are sufficiently high to accommodate the easier flow of material during the FSW process. Another important observation with the temperature plots was that the peak temperature reached at all the three thermocouple locations for both the materials were similar and within a very small range, indicating that the microstructural evolution throughout the weld bead would remain consistent (Fig. 4 (a1 and b1)). Therefore, conducting microstructural investigation and characterizing the mechanical properties at any cross-section or region along the welds would yield results relevant to the entire welded region. This assumption will be used to draw general conclusions based on site-specific observations made in the subsequent sections of this paper.

3.2. Clamping and welding of the jacket sections

With the FSW process parameters narrowed down for both the materials, the next step was to design suitable clamping fixtures to firmly secure the jacket web sections while joining them. A total of four different welds would be required to form the complete jacket around the cable. The clamping approach involved the utilization of a machined AL6XN plate to hold a hardened steel mandrel which supported the curved geometry of the jacket web sections. The schematic representations of the front view and the top view images of the clamping methodology used for all four welds needed to create a complete jacket are shown in Fig. 3 (a, b, and c). The first three welds were supported by a hardened M2 stainless steel mandrel with 19.56 mm diameter (McMaster-Carr, Santa Fe Springs, CA) while the fourth weld was supported by the VIPER cable wrapped in an austenitic stainless-steel shim. The weld appearances of all four jacket welds corresponding to both the materials are shown in Fig. 5 (a). The welds supported by the mandrel had enough backing force to obtain full penetration welds with no defects. However, the final weld (weld 4), which was supported by the copper cable, had both surface and sub-surface defects (Fig. 5 a, b, c). The reason for the surface defects present in weld 4 of both the materials was due to the presence of ridges in the cable section where there was no backing force to support the weld as it was being made. The sub-surface defects in weld 4 for both the SS 316 LN jacket and N50 jacket as observed in Fig. 5 (b and c) were caused due to the soft nature of the copper cable not being able to sufficiently support and provide the backing reaction forces needed during the FSW run. Both the surface and sub-surface defects would be bad considering the application. The defective welds would possess weaker mechanical properties

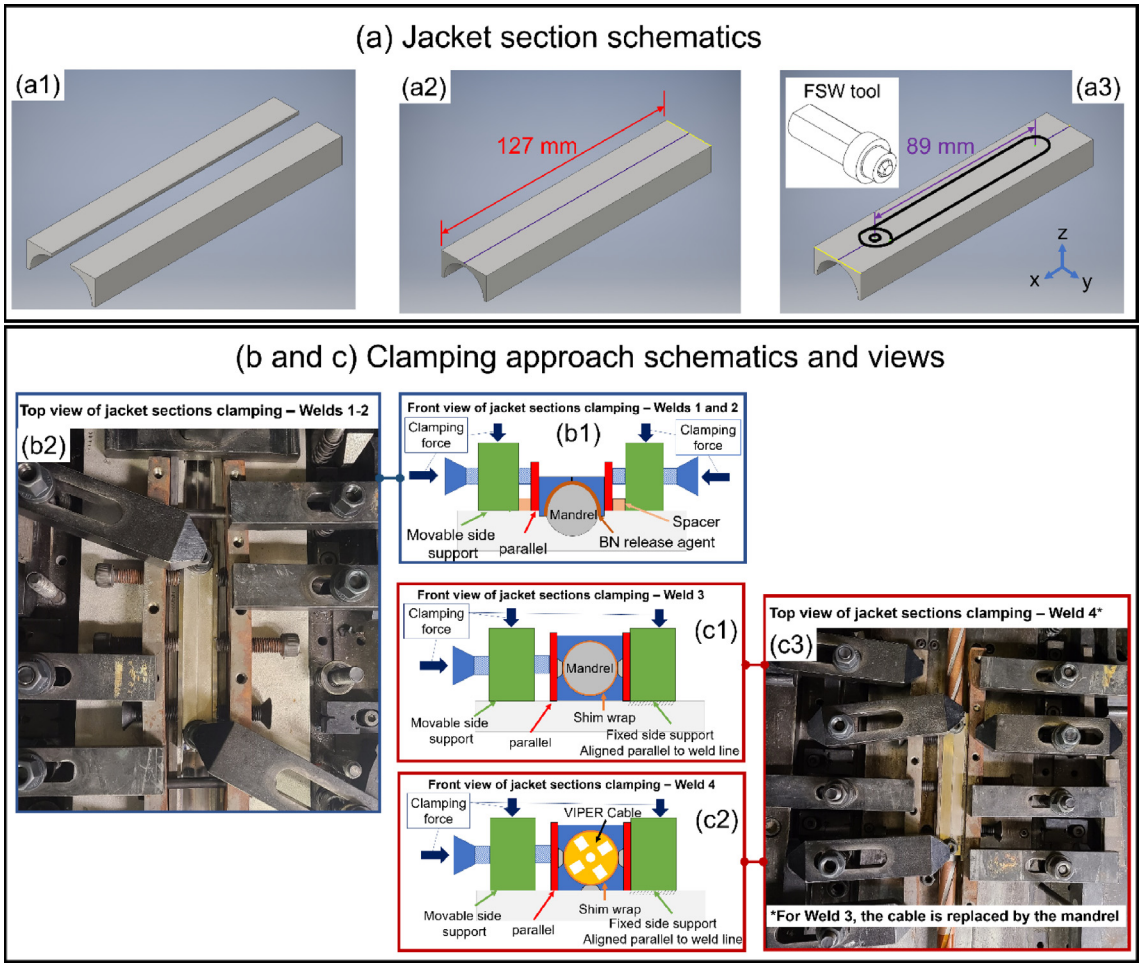

Fig. 3. (a) Jacket sections schematics, (b) & (c) schematics and views of the clamping approach.

and create adverse effects when the cable is magnetized. This would rule out the possibility of utilizing this approach during the manufacture of jackets for the Toroidal Field and Poloidal Field cables. One solution to overcome these welding defects would be to make the fourth weld which is also supported by a mandrel as well and then insert the cable inside the complete jacket/conduit.

3.3. Macro and microstructural characterization of the welds

After making all four welds on the jacket sections with both the materials, macro and microstructural investigations of all four welds were carried out. To be inclusive to both the materials and all four welds, representative regions for characterization were taken from both the welded jacket materials covering all the bases to give a complete picture. Fig. 5 (b) shows a complete cross section of the jacket on cable arrangement after all four welds were made on the SS 316 LN material. Welds 1–3, which were supported by the mandrel, were defect-free, full penetration welds, whereas the fourth weld had a sub-surface defect at the bottom of the stir zone/weld nugget due to insufficient backing force provided by the copper cable. Fig. 6 (a) shows weld 1 or 2 (since both welds are identical in nature with the clamping setup) of the SS 316 LN material starting from the macro-scale down to the micro-scale. Fig. 6 (a2, b2) show the etched optical micrographs for both the welded jacket materials with the different regions of the weld delineated – the central stir zone (SZ) or weld nugget, the thermo-mechanically affected zone (TMAZ), the heat-affected zone (HAZ), and the base material (BM). Fig. 6 (a3, a4) show the inverse pole figure maps of regions within the SS 316 LN base material (BM) and the stir zone (SZ), respectively. The BM consisted of strain-free grains with an average grain size of 16.3 ± 5.6 μm and after welding, the region in the middle of the SZ had an average grain size of 2 ± 0. 9 μm. There was a significant refinement of grains within the SZ due to the process of dynamic recrystallization (DRXZ) occurring during the FSW process. The mechanisms of DRXZ during FSW of nitrogen-containing stainless steels and other alloys are explained elsewhere [32–35]. Within the SZ, there was a bimodal distribution of strain-free grains which indicates that the recrystallization process occurred at different rates in different regions of the processed material and hence led to a larger extent of grain growth of some grains as opposed to others. Having a bimodal grain size distribution would be beneficial to attain a good synergy between strength and ductility [36].

Fig. 6 (b) shows weld 3 of N50 material and beneath the welded jacket, the cable wrapped in shim material is also visible. Like weld 1 or 2 of SS 316 LN, weld 3 of N50 was also defect-free and had a full penetration. Fig. 6 (b1-b4) show corresponding regions of the third weld similar to Fig. 6 (a1 -a4). It was observed that the N50 BM had a finer average grain size of 7.1 ± 3.6 μm as compared to the 16.3 μm average grain size of the SS 316 LN material. After welding, the average grain size in the SZ was refined to 1.2 ± 0.8 μm with a bimodal distribution similar to what was observed in the SS 316 LN SZ. The grain refinement mechanism during FSW of N50 is also similar to that of SS 316 LN which follows the DRXZ route.

Weld 4 of both the SS 316 LN in Fig. 5 (b) and N50 in Fig. 5 (c) had a sub-surface defect at the bottom of the weld nugget apart

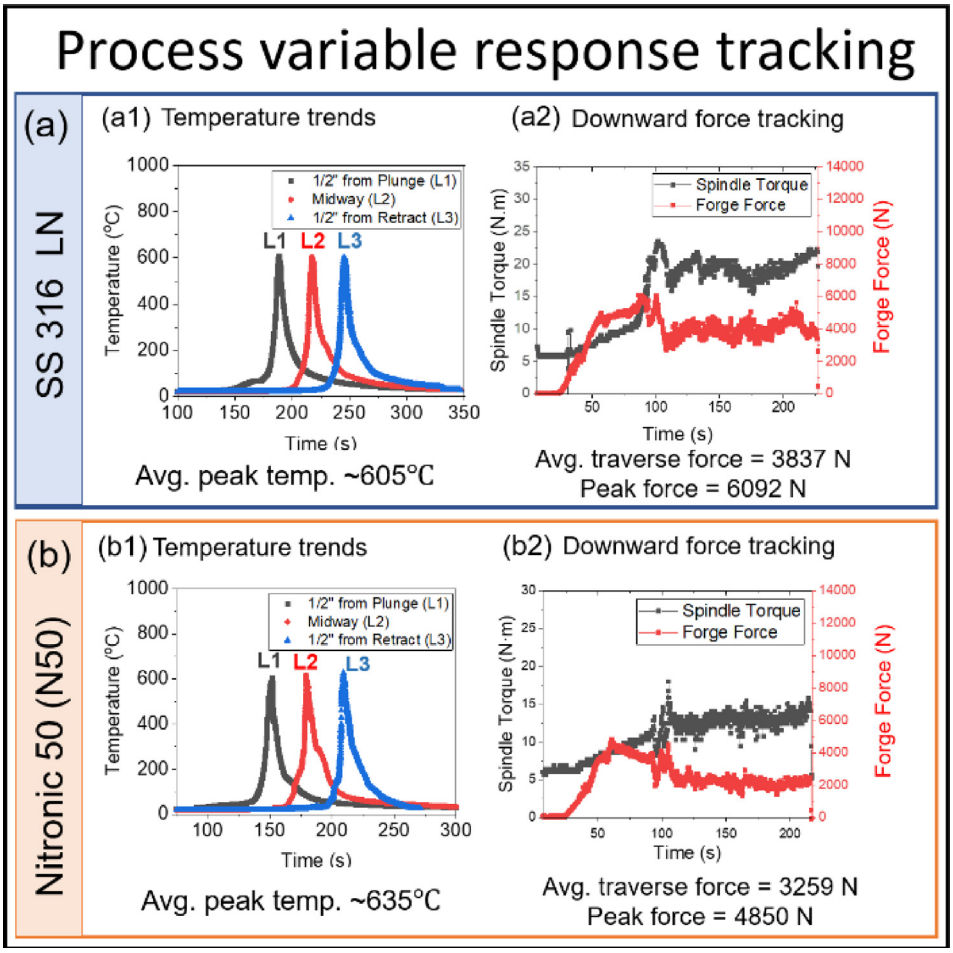

Fig. 4. Temperature and downward force tracking, (a) for SS 316 LN FSW run, and (b) for N50 FSW run.

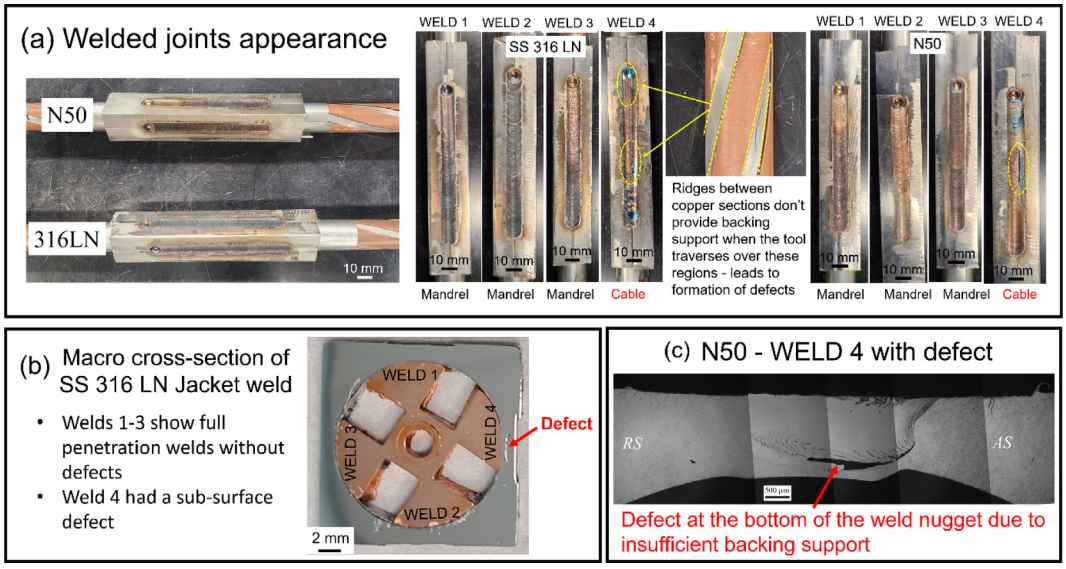

Fig. 5. (a) Appearance of welded joints for both the SS 316 LN and N50 jackets, (b) macro cross-section of the SS 316 LN jacket weld, and (c) weld 4 of the N50 jacket showing a sub-surface defect.

from the surface defect as observed in Fig. 5 (a). The sub-surface defect was caused due to insufficient backing force provided by the copper cable supporting the FSW run as copper is an exceedingly soft material when compared with the hardened stainless steels mandrel. The general rule of thumb is to use much harder backing plates as compared to the workpiece material to avoid these kinds of sub-surface defects. However, since the initial optimization was geared towards lowering the downward forge forces acting on the material, an attempt was made with weld 4 supported by the copper cable, which proved to be unsuccessful. The

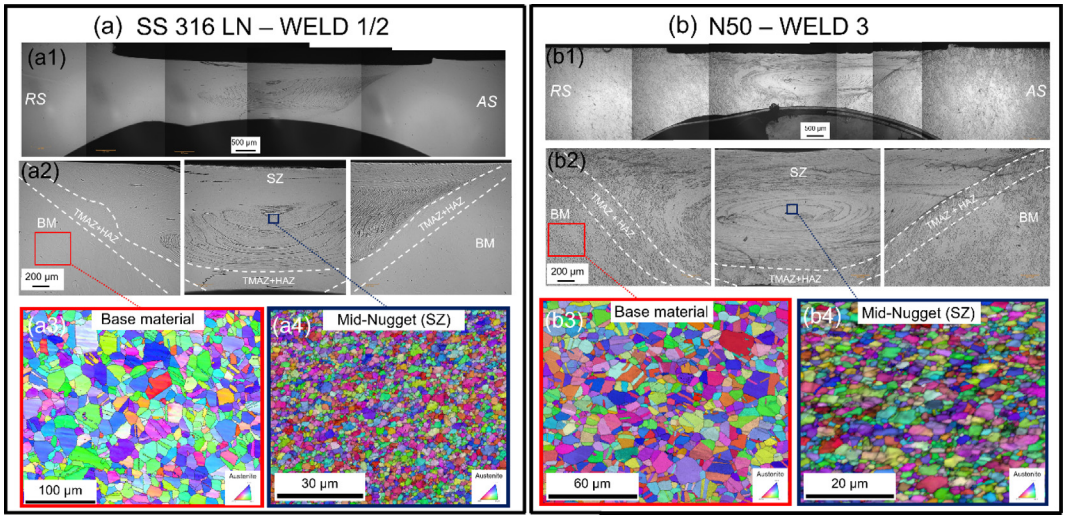

Fig. 6. Macro and micrographs of welds 1–3 with representing the SS 316 LN welded jacket (a, b) and the N50 welded jacket (c, d).

motivation behind this approach was to reduce one step in the manufacturing process of these jackets which did not work out well in this case. However, this issue can be addressed by changing the approach where weld 4 is also made with a hardened steel mandrel providing backing support, similar to welds 1–3, and the cable wrapped in protective shims being inserted into the fully formed jacket with all four welds already made. This approach will help mitigate the surface defects that were observed in Fig. 5 as well due to the ridges being absent on a hardened steel mandrel. Essentially, with the newer approach, all four welds are supported by a hardened steel mandrel.

3.4. Hardness line profiles along the mid-region of the welds

Hardness line profiles of the weld were generated with a Vickers microhardness indenter along the mid-way line of both materials to track the change in hardness from the BM to the SZ on both the advancing side and retreating side of the welds. It was observed that the SS 316 LN BM had an average hardness of 172 ± 4 $HV_{0.1}$ and the SZ had an average hardness of 240 ± 10 $HV_{0.1}$. The hardness within the TMAZ + HAZ region was between the BM and the SZ indicating that there were no unwanted, weakening phases forming in that region. The increased hardness in the SZ region is due to the presence of a refined bimodal microstructure which would offer higher resistance to dislocation motion as compared to the coarser grained BM. Fig. 7 (a) shows the hardness line profile plot for the SS 316 LN material.

Similarly, the hardness line profile for the N50 weld was also plotted and presented in Fig. 7 (b). The N50 BM had an average hardness of 243 ± 5 $HV_{0.1}$ and the SZ had an average hardness of 285 ± 10 $HV_{0.1}$. Both the BM and the SZ of N50 were harder than that of the BM and SZ of the SS 316 LN material due to the finer grain size and presence of a higher fraction of substitutional solute atoms increasing the impeding forces to dislocation motion [37]. Also, the TMAZ + HAZ region had an intermediate hardness range between the BM and SZ indicating that there were no unwanted phases evolving in the N50 material as well.

In general, FSW had a positive impact on the material properties by strengthening the SZ in both the materials while avoiding the evolution of undesirable weakening phases in the TMAZ and HAZ. This unique advantage is a result of the nature of the FSW process which involves severe plastic deformation accompanied by dynamic recrystallization and cannot be achieved with traditional fusion welding [38]. Due to the dimensions of the welded jacket, transverse tensile specimens were not possible for computation of joint efficiency. However, previous reports on FSW of austenitic stainless steels that reported defect free welds with similar increase in hardness in the weld nugget as seen in the present study also reported joint efficiencies of 100% where the tensile specimens were fracturing in the base material region within the gage sections [39]. The asymmetry in the hardness line profiles within the SZ indicate the presence of so-called band structures which resulted from the wear of the tool probe during FSW. These band structures can be seen on the AS side of the SS 316 LN SZ (Fig. 6 (a2)) and on the RS of the N50 SZ (Fig. 6 (b2)). The hardness values in the regions where the band structures were present were higher than the other regions within the SZ as seen in Fig. 7 (a) and (b). The band structure formation was the result of worn particles from the rotating tool that were deposited in an alternating layer-wise fashion within the SZ. In-depth discussion on the formation mechanism of these band structures during FSW of austenitic stainless steels with W-Re tooling can be found elsewhere [33].

3.5. Tensile behavior

To further characterize the mechanical properties of the two welded materials, tensile tests were carried out using mini-tensile samples milled out from the FSW SZ and the BM. The samples were machined out of the jackets in a way that the gauge sections corresponded to the SZ (Fig. 1 (d)) and the BM were being evaluated. The images of fractured tensile specimens are presented in Fig. 8 (a). The engineering stress–strain curves for the SS 316 LN and N50 materials are presented in Fig. 8 (b) for the corresponding FSW and BM regions, respectively. The yield strength, ultimate tensile strength, and plastic elongation for all the tensile tested samples are listed in Table 3.

It was observed that the FSW region corresponding to both the SS 316 LN and N50 materials had a higher yield strength as compared to the BM of the respective samples. This is because of the much finer recrystallized microstructure of the FSW region as compared with the coarser microstructure of the BM region following the Hall-Petch relationship. To understand the deformation and work hardening behavior post yielding of both the materials and corresponding regions within each material, the true stress – strain curves superimposed with the work hardening rate curves were plotted (Fig. 8 (c) and (d)). Apart from the SS 316 LN BM sample, all the other three samples displayed similar work hardening behavior which is explained by the formation of twins during the

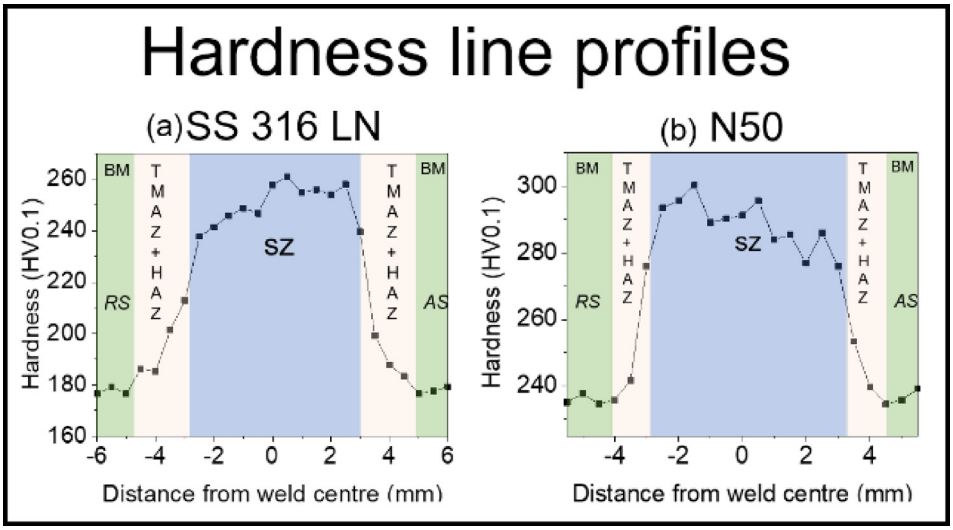

Fig. 7. Hardness line profiles along the mid sections of the (a) SS 316 LN, and (b) N50 jacket welds.

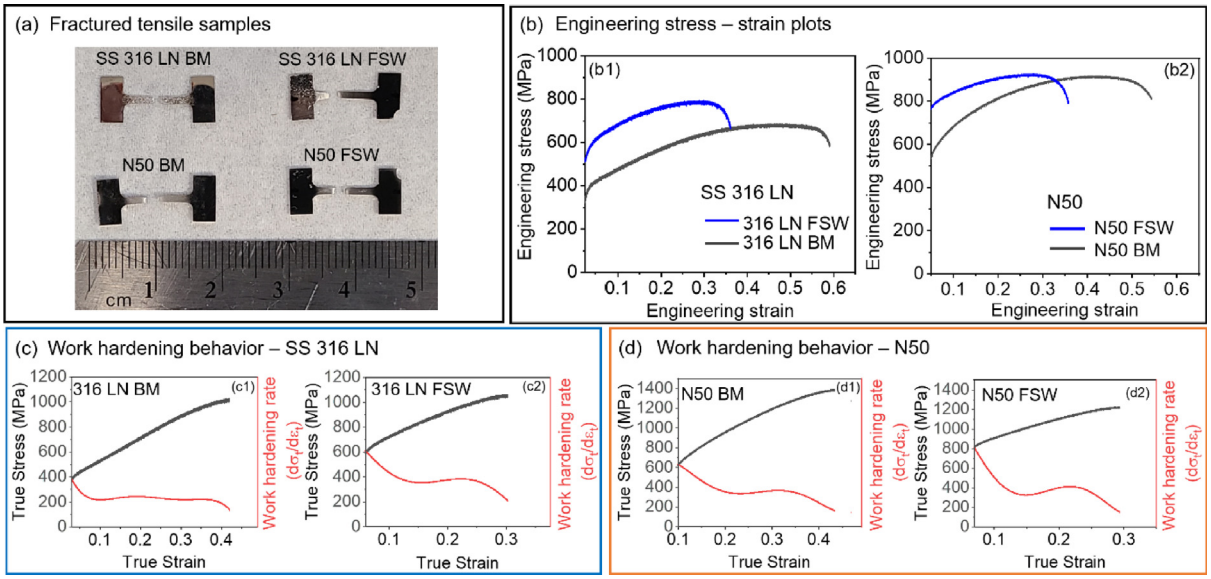

Fig. 8. (a) Fractured tensile specimens, (b) engineering stress–strain plots of BM and FSW region of SS 316 LN (b1) and N50 (b2), (c) true stress–strain response and work hardening response of BM (c1) and FSW region (c2) of SS316 LN, and (d) true stress–strain response and work hardening response of BM (d1) and FSW region (d2) of N50.

Table 3
Tensile properties of BM and FSW section in both SS 316 LN and N50.

Sample/ region	Yield strength (MPa)	Ultimate tensile strength (MPa)	Plastic elongation (%)
SS 316 LN BM	340 ± 5	686 ± 8	56 ± 3
SS 316 LN FSW	513 ± 7	794 ± 11	33 ± 2
N50 BM	536 ± 21	916 ± 17	49 ± 4
N50 FSW	766 ± 19	927 ± 11	31 ± 2

plastic deformation of these austenitic stainless steels [40]. With the SS 316 LN BM sample, it was observed that there were two local minimas within the work hardening curve indicating the presence of two different modes of deformation at different strain levels. This type of behavior was elucidated in Masumura et al. [41] where they explain that the initial part of the plastic deformation proceeds via the formation of deformation twins, but beyond a certain amount of strain, martensitic transformation occurs in the regions between the deformation twins allowing further plastic deformation and work hardening. Misra et al. [42] explained that this phenomenon (twinning + martensitic transformation) is prominently observed in austenitic stainless steels only when the initial grain size of the material before the onset of plastic deformation is large enough to accommodate both the modes of deformation which was the case with the SS 316 LN BM region. However, the SS 316 LN FSW, N50 BM, and N50 FSW regions had significantly finer grain sizes to start with and therefore could not accommodate noticeable enough martensitic transformation to be reflected on the work hardening curves as observed during the later stages of plastic deformation of the SS 316 LN BM region.

3.6. Magnetic properties

To evaluate how well the welded jackets would perform during the application, which would involve cryogenic service temperatures and very high-intensity magnetic fields passing through

them, the magnetic properties were evaluated at three critical locations within each of the welded jackets encompassing all the possible microstructural variations within the samples. All the samples had a mass of 0.15 ± 0.02 g to keep the measurements consistent for comparison. The three distinct regions of the samples tested were the SZ, BM, and TZ (which had regions from the SZ, TMAZ, HAZ, and BM). The magnetization, M (emu/g) v/s temperature at a constant applied magnetic field, H = 500 Oe, ranging from temperature, T = 5 K to 300 K along with the magnetization, M (emu/g) v/s applied magnetic field, H, at T = 5 K, 77 K, and 300 K were evaluated for the three distinct regions from both the welded jackets. The magnetic properties corresponding to the SS 316 LN material are presented in Fig. 9.

The general observation for all the three distinct regions, SZ, BM, and TZ, was that they all displayed a paramagnetic response, which is what is ideally required during application. Even though there is a certain extent of magnetization at temperatures < 100 K as indicated by the small coercivity of the samples (~200 Oe), all three regions show the same behavior and the 316 LN BM used in this experiment is rated to be utilized for jacket application and both the SZ and TZ regions show almost identical behavior and hence would also qualify for usage in a nuclear fusion reactor. The increase in the degree of magnetization at lower temperatures is associated with the ability of some dipole domains to retain their orientation after the applied magnetic field is removed. There is some degree of magnetization of the γ-austenite phase at temperatures < 100 K. However, this phenomenon is observed across all the three distinct regions analyzed and therefore is suitable for the application.

The magnetic properties recorded for the N50 jacket at the three distinct regions did not line up as they did with the SS 316 LN jacket. The SZ region displayed a sharp increase in the magnetization behavior as compared to the BM and TZ regions. This was an indication that there were some microstructural modifications happening in this region leading to the distinctly different observed behavior in magnetic response. Such a variation in magnetic behavior suggests that the SZ region contained some fraction of ferromagnetic phases which could be either α-ferrite or δ-ferrite. To further evaluate the microstructure, high-resolution EBSD scans were carried out at different regions within the SZ of the N50 welded jacket. It was observed that there was the presence of δ-ferrite at the bottom of the SZ as shown in the phase map in Fig. 10.

Due to the presence of some fraction of δ-ferrite formed during the FSW process within the SZ of the N50 welded jacket, the SZ region displayed a more pronounced ferromagnetic behavior during magnetic testing. The formation of δ-ferrite at the bottom of the SZ during FSW can be attributed to the faster cooling rates in this region as it is closest to the backing mandrel which acts as a

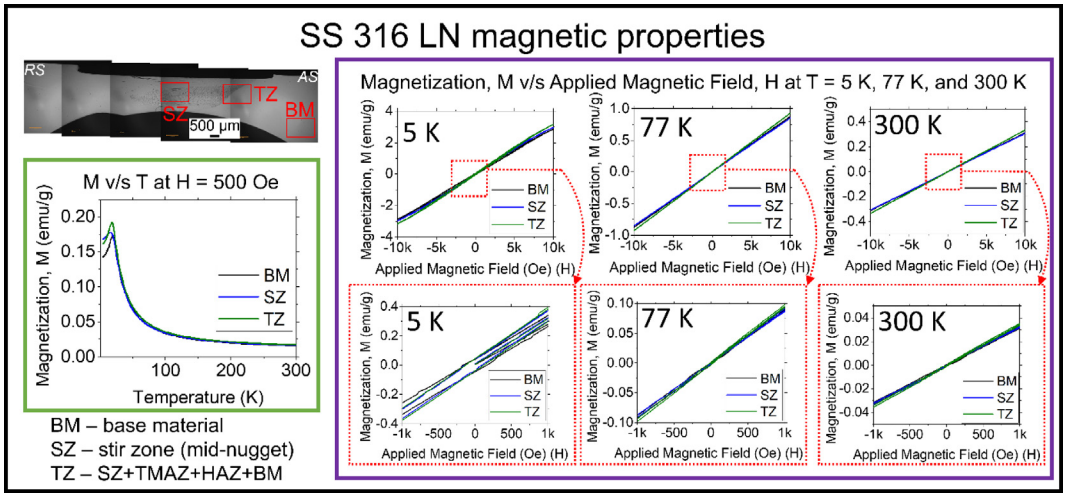

Fig. 9. Magnetic properties magnetization (M) v/s temperature (T), and magnetization (M) v/s applied magnetic field (H) for the SS 316 LN jacket.

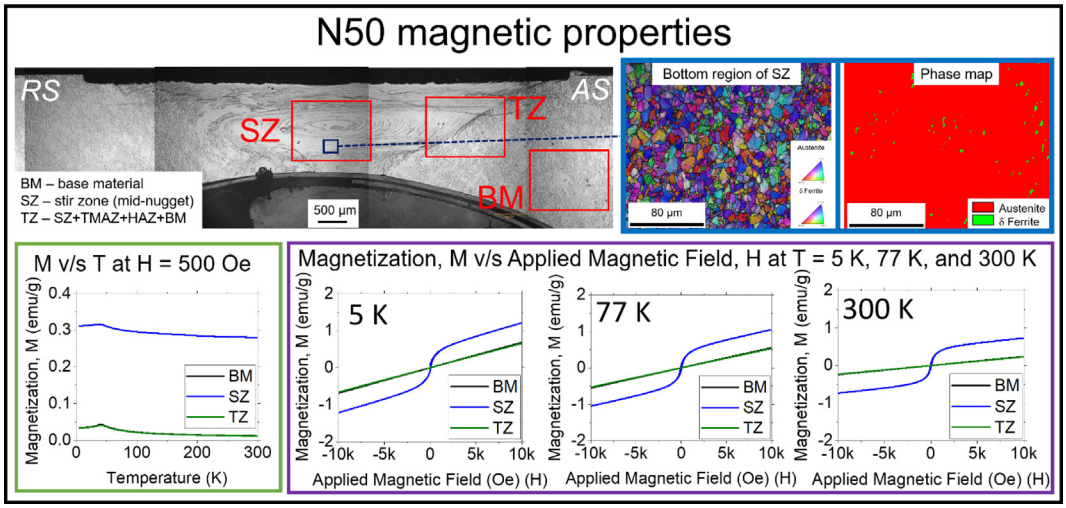

Fig. 10. Magnetic properties magnetization (M) v/s temperature (T), and magnetization (M) v/s applied magnetic field (H) for the N50 jacket.

heat sink. Due to the higher cooling rates, the residence time at elevated temperatures where dynamic recrystallization is active is very low leading to some regions not being able to recrystallize and form new strain-free austenitic grains. There are reports of the formation of δ-ferrite and martensite during the cold deformation of high Mn steels. Nitronic 50 can be considered as a high Mn steel with 4–6 wt% Mn [33,43]. The ferromagnetic behavior of the SZ region would not be ideal during application which requires the material to be as close to a perfect paramagnetic material as possible. Therefore, the N50 welded jacket would not be suitable for application as a FSW welded jacket material in nuclear fusion devices.

4. Conclusions

A friction stir welding approach was adopted to join jacket web sections of SS 316 LN and Nitronic 50 materials for cable-in-conduit conductor application in supercritical nuclear reactor systems. Broad conclusions drawn from the effort are listed below:

a. The feasibility of FSW to join jacket web sections for CICC applications is demonstrated – the overall approach consisted of four welds to form the jacket.
b. The first three welds (welds 1–3), which were supported by a hard backing mandrel, were full penetration welds and defect-free for both the materials, but weld-4, which was made directly on the cable, had both surface and subsurface defects due to the soft nature of the copper material and the ridges present on the cable.
c. It is suggested that these defects can be avoided by making the fourth weld also on the hard backing mandrel material and then inserting the cable into the fully formed jacket.
d. The SS 316 LN welded jacket possessed the ideal set of mechanical and magnetic properties which are critical to the application.
e. The weld nugget (SZ) region of the N50 welded jackets had some fraction of δ-ferrite phase which made its magnetic behavior unsuitable for the application.

CRediT authorship contribution statement

Supreeth Gaddam: Conceptualization, Methodology, Investigation, Data curation, Formal analysis, Writing – original draft. **Ravi Sankar Haridas:** Methodology, Investigation, Formal analysis, Writing – review & editing. **Charlie Sanabria:** Methodology, Formal analysis, Writing – review & editing. **Deepthi Tammana:** Methodology, Formal analysis, Writing – review & editing. **Diana Berman:** Methodology, Investigation, Writing – review & editing. **Rajiv S. Mishra:** Conceptualization, Project administration, Resources, Supervision, Writing – review & editing.

Data availability

Data will be made available on request.

Declaration of Competing Interest

The authors declare that they have no known competing financial interests or personal relationships that could have appeared to influence the work reported in this paper.

Acknowledgments

The authors thank Commonwealth Fusion Systems (CFS), Cambridge MA for providing funding to carry this research out at the Center for Friction Stir Processing (CFSP) and the Advanced Materials and Manufacturing Institute (AMMPI) within the University of North Texas (UNT), Denton TX. The authors thank Dr. Christopher Lammi and Dr. Dan Brunner from CFS for providing valuable comments while preparing the manuscript. The authors also thank the Materials Research facility (MRF) for access to the microscopy facility at UNT. The authors finally thank Dr. Dwight Burford (Joining Innovations, LLC, Wichita, KS) for helping with tool preparation and Mr. Richard Pierson, manager at the Engineering Manufacturing Facility (EMF) at UNT, for helping with the machining and setup to accomplish the welds.

References

[1] N.J. Fisch, Confining a tokamak plasma with rf-driven currents, Phys. Rev. Lett. 41 (1978) 873–876, https://doi.org/10.1103/PhysRevLett.41.873.
[2] V. Barabash, A. Peacock, S. Fabritsiev, G. Kalinin, S. Zinkle, A. Rowcliffe, J.W. Rensman, A.A. Tavassoli, P. Marmy, P.J. Karditsas, F. Gillemot, M. Akiba, Materials challenges for ITER - Current status and future activities, J. Nucl. Mater. 367-370 A (2007) 21–32. 10.1016/j.jnucmat.2007.03.017.
[3] A.J. Creely, M.J. Greenwald, S.B. Ballinger, D. Brunner, J. Canik, J. Doody, T. Fülöp, D.T. Garnier, R. Granetz, T.K. Gray, C. Holland, N.T. Howard, J.W. Hughes, J.H. Irby, V.A. Izzo, G.J. Kramer, A.Q. Kuang, B. Labombard, Y. Lin, B. Lipschultz, N.C. Logan, J.D. Lore, E.S. Marmar, K. Montes, R.T. Mumgaard, C. Paz-Soldan, C. Rea, M.L. Reinke, P. Rodriguez-Fernandez, K. Särkimäki, F. Sciortino, S.D. Scott, A. Snicker, P.B. Snyder, B.N. Sorbom, R. Sweeney, R.A. Tinguely, E.A. Tolman, M. Umansky, O. Vallhagen, J. Varje, D.G. Whyte, J.C. Wright, S.J. Wukitch, J. Zhu, Overview of the SPARC tokamak, J. Plasma Phys. (2020) 1–25, https://doi.org/10.1017/S0022377820001257.
[4] W. Manheimer, Two heretical thoughts on fusion and climate, Energy Environ. 27 (2016) 765–784, https://doi.org/10.1177/0958305X16674636.
[5] D. Badrinarayan, Environmental Challenges of Climate-Nuclear Fusion: A Case Study of India, UCLA J. Environ. Law Policy. 29 (2011), https://doi.org/10.5070/l5291019963.
[6] S. Pradhan, Y. Saxena, A.V. Krivykh, Cable-in-Conduit Conductor for Superconducting Magnets of SST-1 Tokamak, IAEA Tech, Comm. Meet. Steady-State Oper. Magn. Fusion Devices. (1999) 482.
[7] P. Bruzzone, 30 Years of conductors for fusion: A summary and perspectives, IEEE Trans. Appl. Supercond. 16 (2006) 839–844, https://doi.org/10.1109/TASC.2006.873342.
[8] N. Mitchell, A. Devred, P. Libeyre, B. Lim, F. Savary, The ITER magnets: Design and construction status, IEEE Trans. Appl. Supercond. 22 (2012), https://doi.org/10.1109/TASC.2011.2174560.
[9] P.H. Liu, Z.H. Mao, J.G. Qin, C. Dai, H. Jin, L. Li, K. Wang, H. Ji, S. Liu, Research on the mechanical properties of jacket used for Bi-2212 cable-in-conduit conductor, IEEE Trans. Appl. Supercond. 27 (2017) 1–4, https://doi.org/10.1109/TASC.2017.2652058.
[10] Z.S. Hartwig, R.F. Vieira, B.N. Sorbom, R.A. Badcock, M. Bajko, W.K. Beck, B. Castaldo, C.L. Craighill, M. Davies, J. Estrada, V. Fry, T. Golfinopoulos, A.E. Hubbard, J.H. Irby, S. Kuznetsov, C.J. Lammi, P.C. Michael, T. Mouratidis, R.A. Murray, A.T. Pfeiffer, S.Z. Pierson, A. Radovinsky, M.D. Rowell, E.E. Salazar, M. Segal, P.W. Stahle, M. Takayasu, T.L. Toland, L. Zhou, VIPER: An industrially scalable high-current high-temperature superconductor cable, Supercond. Sci. Technol. 33 (2020), https://doi.org/10.1088/1361-6668/abb8c0.
[11] R.L. Tobler, A. Nishimura, J. Yamamoto, Design-relevant mechanical properties of 316-type steels for superconducting magnets, Cryogenics (Guildf). 37 (1997) 533–550, https://doi.org/10.1016/S0011-2275(97)00071-4.
[12] P. Decool, D. Ciazynski, A. Nobili, S. Parodi, P. Pesenti, A. Bourquard, F. Beaudet, Joints for large superconducting conductors, Fusion Eng. Des. 58–59 (2001) 123–127, https://doi.org/10.1016/S0920-3796(01)00408-2.
[13] K. Takahata, T. Mito, H. Tamura, S. Imagawa, A. Sagara, Conceptual design of an indirect-cooled superconducting magnet for the LHD-type fusion reactor FFHR, Fusion Eng. Des. 82 (2007) 1487–1492, https://doi.org/10.1016/j.fusengdes.2007.04.050.
[14] M.F. McGuire, Austenitic Stainless Steels, Encycl. Mater. Sci. Technol. (2001) 406–410, https://doi.org/10.1016/b0-08-043152-6/00081-4.
[15] J.H. Kim, J. Feng, The 4k mechanical properties of modified SS316lN for jacket materials in superconducting fusion magnets, AIP Conf. Proc. 986 (2008) 92–99, https://doi.org/10.1063/1.2900401.
[16] S.T.S. Teels, Materials for Cryogenic Service: Engineering Properties of Austenitic Stainless Steels, Nickel Dev. Inst. (1974).
[17] D.C. Larbalestier, H.W. King, Austenitic stainless steels at cryogenic temperatures 1-Structural stability and magnetic properties, Cryogenics (Guildf). 13 (1973) 160–168, https://doi.org/10.1016/0011-2275(73)90285-3.
[18] K. Kim, H.K. Park, K.R. Park, B.S. Lim, S.I. Lee, Y. Chu, W.H. Chung, Y.K. Oh, S.H. Baek, S.J. Lee, H. Yonekawa, J.S. Kim, C.S. Kim, J.Y. Choi, Y.B. Chang, S.H. Park, D. J. Kim, N.H. Song, K.P. Kim, Y.J. Song, I.S. Woo, W.S. Han, S.H. Lee, D.K. Lee, K.S. Lee, W.W. Park, J.J. Joo, H.T. Park, S.J. An, J.S. Park, G.S. Lee, Status of the KSTAR superconducting magnet system development, Nucl. Fusion. 45 (2005) 783–789, https://doi.org/10.1088/0029-5515/45/8/003.
[19] K.H. Tseng, Study on surface appearance, geometry size, and delta-ferrite content of ZrO2-aided TIG welding of AISI 316LN stainless steel, Int. J. Adv.

Manuf. Technol. 89 (2017) 2355–2362, https://doi.org/10.1007/s00170-016-9280-2.
[20] G. Dak, C. Pandey, A critical review on dissimilar welds joint between martensitic and austenitic steel for power plant application, J. Manuf. Process. 58 (2020) 377–406, https://doi.org/10.1016/j.jmapro.2020.08.019.
[21] C. Pandey, Mechanical and Metallurgical Characterization of Dissimilar P92/SS304 L Welded Joints Under Varying Heat Treatment Regimes, Metall. Mater. Trans. A Phys. Metall. Mater. Sci. 51 (2020) 2126–2142, https://doi.org/10.1007/s11661-020-05660-0.
[22] G. Dak, S. Sirohi, C. Pandey, Study on microstructure and mechanical behavior relationship for laser-welded dissimilar joint of P92 martensitic and 304L austenitic steel, Int. J. Press. Vessel. Pip. 196 (2022), https://doi.org/10.1016/j.ijpvp.2022.104629 104629.
[23] S. Sirohi, P.K. Taraphdar, G. Dak, C. Pandey, S.K. Sharma, A. Goyal, Study on evaluation of through-thickness residual stresses and microstructure-mechanical property relation for dissimilar welded joint of modified 9Cr–1Mo and SS304H steel, Int. J. Press. Vessel. Pip. 194 (2021), https://doi.org/10.1016/j.ijpvp.2021.104557.
[24] A.K. Maurya, C. Pandey, R. Chhibber, Influence of heat input on weld integrity of weldments of two dissimilar steels, Mater. Manuf. Process. 00 (2022) 1–22, https://doi.org/10.1080/10426914.2022.2075889.
[25] C.D. Graham, B.E. Lorenz, Delta ferrite is ubiquitous in type 304 stainless steel: Consequences for magnetic characterization, J. Magn. Magn. Mater. 458 (2018) 15–18, https://doi.org/10.1016/j.jmmm.2018.02.092.
[26] D.G. Mohan, C.S. Wu, A Review on Friction Stir Welding of Steels, Chinese J. Mech. Eng. (English Ed.) 34 (2021), https://doi.org/10.1186/s10033-021-00655-3.
[27] M. Mahoney, T. Nelson, C. Sorenson, S. Packer, Friction stir welding of ferrous alloys: Current status, Mater. Sci. Forum. 638–642 (2010) 41–46, https://doi.org/10.4028/www.scientific.net/MSF.638-642.41.
[28] F.C. Liu, Y. Hovanski, M.P. Miles, C.D. Sorensen, T.W. Nelson, A review of friction stir welding of steels: Tool, material flow, microstructure, and properties, J. Mater. Sci. Technol. 34 (2018) 39–57, https://doi.org/10.1016/j.jmst.2017.10.024.
[29] P.J. Maziasz, J.T. Busby, Properties of austenitic steels for nuclear reactor applications, Elsevier Inc., 2012. 10.1016/B978-0-08-056033-5.00019-7.
[30] S. Şahin, M. Übeyli, A review on the potential use of austenitic stainless steels in nuclear fusion reactors, J. Fusion Energy. 27 (2008) 271–277, https://doi.org/10.1007/s10894-008-9136-3.
[31] M. Komarasamy, R.S. Mishra, Serration behavior and shear band characteristics during tensile deformation of an ultrafine-grained 5024 Al alloy, Mater. Sci. Eng. A. 616 (2014) 189–195, https://doi.org/10.1016/j.msea.2014.08.027.
[32] Y. Miyano, H. Fujii, Y. Sun, Y. Katada, S. Kuroda, O. Kamiya, Mechanical properties of friction stir butt welds of high nitrogen-containing austenitic stainless steel, Mater. Sci. Eng. A. 528 (2011) 2917–2921, https://doi.org/10.1016/j.msea.2010.12.071.
[33] H. Li, S. Yang, S. Zhang, B. Zhang, Z. Jiang, H. Feng, P. Han, J. Li, Microstructure evolution and mechanical properties of friction stir welding super-austenitic stainless steel S32654, Mater. Des. 118 (2017) 207–217, https://doi.org/10.1016/j.matdes.2017.01.034.
[34] R. Saravanakumar, T. Rajasekaran, C. Pandey, M. Menaka, Influence of Tool Probe Profiles on the Microstructure and Mechanical Properties of Underwater Friction Stir Welded AA5083 Material, J. Mater. Eng. Perform. (2022), https://doi.org/10.1007/s11665-022-06822-4.
[35] R. Saravanakumar, T. Rajasekaran, C. Pandey, M. Menaka, Mechanical and Microstructural Characteristics of Underwater Friction Stir Welded AA5083 Armor-Grade Aluminum Alloy Joints, J. Mater. Eng. Perform. (2022), https://doi.org/10.1007/s11665-022-06832-2.
[36] X. Wu, Y. Zhu, Heterogeneous materials: a new class of materials with unprecedented mechanical properties, Mater. Res. Lett. 5 (2017) 527–532, https://doi.org/10.1080/21663831.2017.1343208.
[37] T.R. Smith, J.D. Sugar, C. San Marchi, J.M. Schoenung, Strengthening mechanisms in directed energy deposited austenitic stainless steel, Acta Mater. 164 (2019) 728–740, https://doi.org/10.1016/j.actamat.2018.11.021.
[38] R.S. Mishra, Z.Y. Ma, Friction stir welding and processing, Mater. Sci. Eng. R Reports. 50 (2005), https://doi.org/10.1016/j.mser.2005.07.001.
[39] T. Ishikawa, H. Fujii, K. Genchi, S. Iwaki, S. Matsuoka, K. Nogi, High speed high quality FSW of ASS_Ishikawa_2009, 49 (2009) 897–901.
[40] K.K. Singh, Strain hardening behaviour of 316L austenitic stainless steel, Mater. Sci. Technol. 20 (2004) 1134–1142, https://doi.org/10.1179/026708304225022089.
[41] T. Masumura, Y. Seto, T. Tsuchiyama, K. Kimura, Work-hardening mechanism in high-nitrogen austenitic stainless steel, Mater. Trans. 61 (2020) 678–684, https://doi.org/10.2320/matertrans.H-M2020804.
[42] R.D.K. Misra, P.K.C. Venkatsurya, M.C. Somani, L.P. Karjalainen, Nanoscale deformation behavior of phase-reversion induced austenitic stainless steels: The interplay between grain size from nano-grain regime to coarse-grain regime, Metall. Mater. Trans. A Phys. Metall. Mater. Sci. 43 (2012) 5286–5297, https://doi.org/10.1007/s11661-012-1360-9.
[43] B. Vijaya Ramnath, C. Elanchezhian, S. Rajesh, S. Jaya Prakash, B.M. Kumaar, K. Rajeshkannan, Design and Development of Milling Fixture for Friction Stir Welding, Mater. Today Proc. 5 (2018) 1832–1838, https://doi.org/10.1016/j.matpr.2017.11.282.